Global instability of compressor stall onset

Shenren Xu [*1], Chen He[†2], Dakun Sun[‡2], and Dingxi Wang[§] [1]

[1]*Northwestern Polytechnical University, Taicang 215400, P.R. China*
[2]*Beihang University, Beijing 100191, P.R. China*

Linear global stability analysis is an effective approach to predict the exact condition at which flow goes unstable. Compared to the time-domain simulation approach, ??? method can equivalently predict the destabilization condition, but at a much lower cost, since unsteady simulations are no longer required. In this work, a Newton–Krylov nonlinear flow solver is used to first solve for the steady state flow solution and then eigenanalysis is performed by applying the implicit-restart Arnoldi method to the exact Jacobian matrix. By tracking a subset of the eigenspectrum that is close to the imaginary axis, the least stable eigenmodes can be found. By perturbing the bifurcation parameter, e.g., the Reynolds number, the Hopf bifurcation point can be identified. This method is applied to find the critical Reynolds number for a laminar flow around a circular cylinder above which laminar vortex shedding appears. Time-accurate unsteady simulation confirms the correctness of the critical eigenvalue and eigenvector found. It is also applied to a quasi-3D compressor rotor annular cascade case, for which eigenanalysis is performed and flow physics is analyzed based on the unstable modes identified. Interesting correlation between the rotating perturbation pattern and cell rotating speed is found, which resembles what is observed in experiments. This work is a first step towards the study of rotating flow instabilities in turbomachines, such as rotating stall and rotating instability, and the preliminery results proved promising for future application to three-dimensional practical problems.

Nomenclature

c_v, c_p	=	specific heat
e	=	internal energy
E	=	total energy
$\partial\Omega_r$	=	boundary of Ω_r

[*]Associate Professor, Yangtze River Delta Research Institute
[†]Ph.D. Candidate, School of Energy and Power Engineering; hechen@buaa.edu.cn
[‡]Associate Professor, School of Energy and Power Engineering; Co-Innovation Center for Advanced Aero-Engine; sundk@buaa.edu.cn
[§]Professor, School of Power and Engery; dingxi_wang@nwpu.edu.cn

I. Introduction

II. Numerical approach

The flow is computed using the NutsCFD solver, whose accuracy has been validated intensively for axial and centrifugal compressors [1]. The RANS equations are discretized using the finite volume method on arbitrary unstructured meshes. The inviscid flux is calculated with Roe's flux difference splitting scheme and the viscous flux is calculated using central scheme. Second-order accurate spatial discretisation is achieved via linear reconstruction of the primitive variable from the mesh node to the flux face center and the gradient of flow variables are obtained using the Green-Gauss approach. Simulation of the unsteady flow for a rotating geometry is converted to the computation of a steady flow by re-formulating the governing equations in a reference frame coindending with the rotating geometry. In order to obtain a steady flow as the base-flow for linearizing the perturbed flow about and performing eigenvalue analysis, at physically unstable states, a globalized Newton–Krylov approach is used to integrate the unsteady RANS equations in time. This is one of the key technical enablers for performing global instability analysis for compressors beyond stall.

The nonlinear flow solver used in this work is NutsCFD, an unstructured-mesh finite-volume RANS solver capable of dealing with rotating frame reference and periodic boundary conditions. The solver features the use of the Newton–Krylov algorithm, which significantly enhances the efficiency and robsutness when computing turbomachinery flows at off-design conditions. Details of the solver can be found in [2] and a brief description of the solution algorithm is provided in this section.

A. Governing equations

The integral form of the governing equations in a relative frame of reference with a constant angular velocity of ω is

$$\frac{d}{dt}\int_{\Omega_r} \mathbf{W}\,dV + \oint_{\partial\Omega_r}(\mathbf{F}_c^r - \mathbf{F}_v)\,dS + \int_{\Omega_r}\mathbf{F}_\omega\,dV = 0,$$

where $\mathbf{W}$ are the conservative variables $[\rho,\ \rho\mathbf{u},\ \rho E]^T$. The absolute and relative convective fluxes, $\mathbf{F}_c$ and $\mathbf{F}_c^r$, the viscous flux $\mathbf{F}_v$, and the additional source term due to rotation, $\mathbf{F}_\omega$, are defined as

$$\mathbf{F}_c = \begin{bmatrix} \rho\mathbf{u}\cdot\mathbf{n} \\ \rho\mathbf{u}\mathbf{u}\cdot\mathbf{n} + p\mathbf{n} \\ \rho H\mathbf{u}\cdot\mathbf{n} \end{bmatrix},\ \mathbf{F}_c^r = \mathbf{F}_c - (\mathbf{u}_{rot}\cdot\mathbf{n})\begin{bmatrix} \rho \\ \rho\mathbf{u} \\ \rho E \end{bmatrix},\ \mathbf{F}_v = \begin{bmatrix} 0 \\ \tau\cdot\mathbf{n} \\ \mathbf{u}\cdot\tau\cdot\mathbf{n} + \kappa\mathbf{n}\cdot\nabla T \end{bmatrix},\ \mathbf{F}_\omega = \begin{bmatrix} 0 \\ \rho\omega\times\mathbf{u} \\ 0 \end{bmatrix},$$

with $\mathbf{u}_{rot} = \omega\times\mathbf{x}$. When ω is zero, a solver applicable to non-rotating reference frame is recovered.

Flow is assumed to be fully turbulent and turbulence is modeled using the negative Spalart–Allmaras (SA-neg) model [3]. Compared to the original SA model [4], this avoids the clipping of the turbulent variable to a non-negative value which potentially prevents the full convergence of the nonlinear solver. The turbulence equation is discretized using the first-order accurate upwind scheme [5].

B. Spatial discretization

The governing equations are discretized using the method of lines and thus the spatial and temporal discretizations can be treated separately. The governing equations for the steady-state solution $\mathbf{W}$ is

$$\mathbf{R}(\mathbf{W}) = \mathbf{0}, \tag{1}$$

where $\mathbf{R}$ is the sum of fluxes and source terms associated with each control volume. Suppose control volume i has N flux faces with area S_{ik} for $k = 1, 2, ..., N$. R_i then is

$$R_i(\mathbf{W}) = \sum_{k=1}^{N}(\mathbf{F}_c^r - \mathbf{F}_v)S_{ik} + \mathbf{F}_\omega V_i,$$

where V_i denotes the volume. The computation of the convective flux $\mathbf{F}_c^r$ is based on a modification of the Roe flux scheme to account for the relative reference frame that is rotating with a constant angular velocity; while the viscous flux $\mathbf{F}_v$ is the same as in the stationary reference frame.

3

C. Temporal discretization for steady solver

The Newton method solves the steady-state nonlinear equation (1) iteratively as

$$\mathbf{W}^{n+1} = \mathbf{W}^n + \beta \Delta \mathbf{W}$$

until convergence is reached, i.e., $\|\mathbf{R}(\mathbf{W})\| = 0$, where $\Delta \mathbf{W}$ is the solution to the linear system of equations

$$\frac{\partial \mathbf{R}}{\partial \mathbf{W}} \Delta \mathbf{W} = -\mathbf{R}(\mathbf{W}^n),$$

while β is an under-relaxation factor obtained using a line search.

Once the spatial discretization, $\mathbf{R}(\mathbf{W}^n)$, is established, there are three main steps to complete a Newton update step, namely, (i) forming the Jacobian matrix, (ii) solving the large sparse linear system of equations, and (iii) finding a step size β and update the nonlinear flow solution. To form the Jacobian matrix, automatic differentiatino tool Tapenade [6] is used, together with graph coloring tool Colpack [7]. By executing the foward-differentiated residual subroutine for a subsets of nodes with the same color, the Jacobian matrix is calculated. The resulting large sparse linear system of equations is solved using GMRES right-preconditioned by the incomplete LU factorization with zero fill-in.

D. Temporal discretization for unsteady solver

III. Global linear stability analysis via eigenmode decomposition

A. Global linear stability analysis

The time-dependent RANS equations, discretized using the method of lines, is of the following form

$$\frac{d\mathbf{u}(t)}{dt} = \mathbf{R}(\mathbf{u}(t)) \tag{2}$$

where $\mathbf{u}(t)$ is vector of the time-varying conservative flow variables and $\mathbf{R}(\mathbf{u})$ is the nonlinear residual representing the spatial discretization. Note that the residual vector has already the volume of the cell taken into account, by diving the sum of the fluxes out of each cell by its volume. Assuming a steady state solution $\mathbf{u}_0$ (equilibrium point of the dynamic system) exists, and the time-varying flow variable can be decomposed into the steady and the unsteady part

$$\mathbf{u}(t) := \mathbf{u}_0 + \tilde{\mathbf{u}}(t)$$

. Assuming the perturbation is small, then and the governing equation becomes

$$\frac{d\tilde{\mathbf{u}}(t)}{dt} = A\tilde{\mathbf{u}}(t)$$

4

where A is the Jacobian $A := \dfrac{\partial \mathbf{R}}{\partial \mathbf{u}}$.

In order to use the eigen model decomposition approach, suppose matrix A has right eigenvectors $\{\mathbf{v}_i, \mathbf{v}_2, ..., \mathbf{v}_N\}$, which forms the matrix V as its colum vectors. Matrix A can then be factorized as

$$A = V\Lambda V^{-1}$$

where the diagonal matrix Λ has the eigenvalues of the matrix A as its diagonal elements. Decomposing the unsteady part $\tilde{\mathbf{u}}$ in the eigen modal space with coordinates $\eta := \{\eta_1, \eta_2, \ldots, \eta_N\}$,

$$\tilde{\mathbf{u}}(t) = V\eta(t).$$

Substituting $\tilde{\mathbf{u}}$ in the governing equation using the eigen modal decomposition, it becomes

$$\frac{d\eta(t)}{dt} = \Lambda\eta(t).$$

All equations are decoupled now and can be written as

$$\frac{d\eta_i(t)}{dt} = \lambda_i \eta_i(t) \quad \forall i.$$

For the linear system to be stable, a sufficient condition is that all eigenvalues have negative real parts, i.e., $\mathrm{real}(\lambda_i) < 0, \forall i$.

B. Relation with time-accurate unsteady analysis

The relation between the eigenvalue and the time-accurate unsteady analysis is discussed in this subsection. Assume that the backward-differentiation-formula 1 (BDF1) is used. The discretized system is then

$$\frac{\eta_i^{n+1} - \eta_i^n}{T} = \lambda_i \eta_i^{n+1} \tag{3}$$

which yields

$$\eta_i^{n+1} = \frac{1}{1 - T\lambda_i} \eta_i^n \tag{4}$$

which means that for η_i to converge to zero, the amplification factor has to have a modulus smaller than 1, i.e.,

$$\left| \frac{1}{1 - T\lambda_i} \right| < 1$$

or equivalently,

$$|1 - T\lambda_i| > 1$$

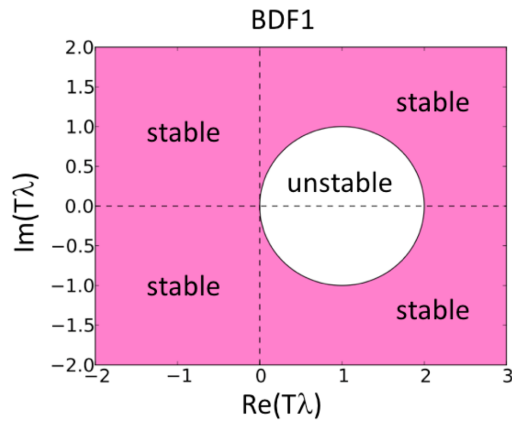The stability region is shown in the red part of the plot in

Fig. 1   123

If BDF2 is used, then the discretized equation becomes

$$\frac{3\eta_i^{n+2} - 4\eta_i^{n+1} + \eta^n}{2T} = \lambda_i \eta_i^{n+2} \tag{5}$$

Assuming the amplication factor is $z \in C$, and substitute $\eta^{n+2} = z^2\eta^n$ and $\eta^{n+1} = z\eta^n$ into eqn, one has the characteristic polynomial that equals zero:

$$(3 + 2T\lambda_i)z^2 - 4z + 1 = 0$$

and the stability region for $T\lambda_i$ can thus be defined as one such that $|z| < 1$, which is visualized in the figure
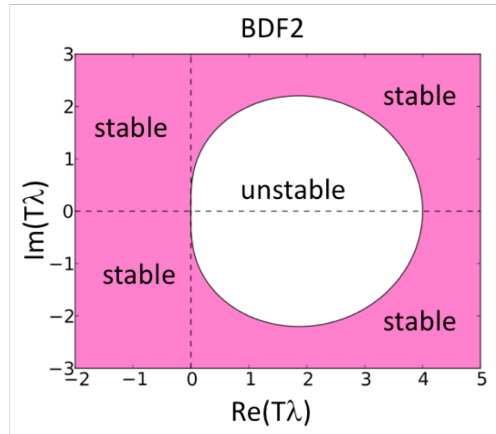

Fig. 2   123

Based on the stability analysis for the 1-step and 2-step backward differentiation formula (BDF), the following conclusions can be drawn regarding its relation to the eigenvalue analysis of the Jacobian matrix A for the spatial discretization.

1) if the matrix A has unstable eigehvalues (those that have positive real parts), then the time-stepping method with a sufficiently small time-step should also exhibit linear instability (eigenvalues of the timestepping matrix lying outside the unit circle).

2) if all eigenvalues of the matrix A have negative real part, then the time-stepping method unconditionally stable, i.e., a small perturbation will decay and diminish.

C. Matrix structure for configurations with cyclic symmetry

1. circulant matrix

Consider the simpliest case of a circulant matrix B

$$B = circ(b_0, b_1, \ldots, b_{M-1}) = \begin{bmatrix} b_0 & b_1 & b_2 & \cdots & b_{M-2} & b_{M-1} \\ b_{M-1} & b_0 & b_1 & \cdots & b_{M-3} & b_{M-2} \\ \vdots & \vdots & \vdots & \vdots & \vdots & \vdots \\ b_1 & b_2 & b_3 & \cdots & b_{M-1} & b_0 \end{bmatrix}$$

Due to the cyclic symmetry, it can be verified that matrix B has M eigenvalues and eigenvectors defined as

$$\mathbf{v}_j = [1, \rho_j, \rho_j^2, \ldots, \rho_j^{M-1}]^T, \; \lambda_j = \sum_{m=0}^{M-1} b_m \rho_j^m \; i = 0, 1, 2, \ldots, M-1$$

Further more, it can be verified that all the eigenvectors are orthogonal to each other.

2. block-circulant matrix

A slightly more complex case is when each element in the circulant matrix is replaced at a block matrix, e.g., b_m is now an $N \times N$ square matrix, resulting in a block-circulant matrix.

Consider a vector $\mathbf{w}$ of the following form:

$$\mathbf{w} = \left[\mathbf{v}, \rho\mathbf{v}, \rho^2\mathbf{v}, \ldots, \rho^{n-1}\mathbf{v}\right]^T$$

where ρ is any M-th root of 1 and $\mathbf{v}$ is a vector of length N.

In order for $\mathbf{w}$ to be the eigenvector of the block-circulant matrix B, the following equation has to be satisfied:

$$B\mathbf{w} = \lambda\mathbf{w}$$

which can be expanded as follows

$$
\begin{aligned}
(b_0 + \rho b_1 + \rho^2 b_2 + \cdots + \rho^{M-1} b_{M-1})\mathbf{v} &= \lambda\mathbf{v} \\
(b_{M-1} + \rho b_0 + \rho^2 b_1 + \cdots + \rho^{M-1} b_{M-2})\mathbf{v} &= \lambda\rho\mathbf{v} \\
(b_{M-2} + \rho b_{M-1} + \rho^2 b_0 + \cdots + \rho^{M-1} b_{M-3})\mathbf{v} &= \lambda\rho^2\mathbf{v} \\
\cdots &= \cdots \\
(b_1 + \rho b_2 + \rho^2 b_3 + \cdots + \rho^{M-1} b_0)\mathbf{v} &= \lambda\rho^{M-1}\mathbf{v}.
\end{aligned}
$$

It can be seen that all rows are identical to the first row, different only by a scalar multiplication. λ and $\mathbf{v}$ can be found by solving the eigenvalue problem of the equation in the first row. There are N $\mathbf{v}$ for each ρ. When ρ varies from ρ_0 to ρ_{M-1}, a total of $N \times M$ $\mathbf{v}$ can be found. The (m,n)-th of them is

$$\mathbf{w}_{m,n} = \left[\mathbf{v}_{m,n}, \rho_m\mathbf{v}_{m,n}, \rho_m^2\mathbf{v}_{m,n}, \ldots, \rho_m^{M-1}\mathbf{v}_{m,n},\right]^T$$

where $\mathbf{v}_{m,n}$ is the n-th eigenvalue of

$$(b_0 + \rho b_1 + \rho^2 b_2 + \cdots + \rho^{M-1} b_{M-1})\mathbf{v} = \lambda\mathbf{v}$$

with $\rho = \rho_m$.

3. linearized discreted RANS equation in axisymmetric domain

The residual vector of the discreted RANS equation $\mathbf{R}$ is linearized with respect to the flow variable $\mathbf{U}$ to arrive at the full Jacobian matrix $\dfrac{\partial\mathbf{R}}{\partial\mathbf{U}}$, which describes the dynamic behavior of the system around the equilibrium point. It turns out that the fact that the computational domain has a cyclic symmetry can be exploited to reveal some characteristics of the eigenspace of the full Jacobian.

To facilate the following discussion, it is assume that the computational mesh, and thus the spatial discretization, is cyclic symmetric with M-periodicity, with M being the number of blades/passages in the entire annulus. Consequently, the full-annulus mesh can be divided into M non-overlapping segments, each of which contains N grid points. The grid points are ordered in such way that points $1 + N \times m$ to $N + N \times m$, $m = 0, 1, 2, \ldots, M - 1$ belongs to the m-th segment. In additional, the location of point $n + N \times m1$ (the n-th point in segment $m1$) is point $n + N \times m2$ (the n-th point in

segment $m2$) rotated by an angle $(m2 - m1) \times 2\pi/M$. The arrangement of the grid point is illustrated in the following figure.

The entire Jacobian matrix then can be partitioned into the following block matrix

$$\frac{\partial \mathbf{R}}{\partial \mathbf{U}} = \begin{bmatrix} \dfrac{\partial \mathbf{R}_0}{\partial \mathbf{U}_0} & \dfrac{\partial \mathbf{R}_0}{\partial \mathbf{U}_1} & \dfrac{\partial \mathbf{R}_0}{\partial \mathbf{U}_2} & \cdots & \dfrac{\partial \mathbf{R}_0}{\partial \mathbf{U}_{M-1}} \\[2mm] \dfrac{\partial \mathbf{R}_1}{\partial \mathbf{U}_0} & \dfrac{\partial \mathbf{R}_1}{\partial \mathbf{U}_1} & \dfrac{\partial \mathbf{R}_1}{\partial \mathbf{U}_2} & \cdots & \dfrac{\partial \mathbf{R}_1}{\partial \mathbf{U}_{M-1}} \\[2mm] \vdots & \vdots & \vdots & \cdots & \vdots \\[2mm] \dfrac{\partial \mathbf{R}_{M-1}}{\partial \mathbf{U}_0} & \dfrac{\partial \mathbf{R}_{M-1}}{\partial \mathbf{U}_1} & \dfrac{\partial \mathbf{R}_{M-1}}{\partial \mathbf{U}_2} & \cdots & \dfrac{\partial \mathbf{R}_{M-1}}{\partial \mathbf{U}_{M-1}} \end{bmatrix} \tag{6}$$

where each block $\dfrac{\partial \mathbf{R}_{m_1}}{\partial \mathbf{U}_{m_2}}$, $m_1, m_2 = 0, 1, \ldots, M-1$, is itself an $5N \times 5N$ matrix for Euler/laminar or $6N \times 6N$ matrix for turbulent flow modelled using a one-equation turbulence model. It can also be seen that each block is non-zero only when m_1 and m_2 either are identical or differ by 1. However, this property is not exploited in this subsection.

By changing the frame of reference to different pitchwise position, it can be shown that the matrix can be rewritten as

$$\frac{\partial \mathbf{R}}{\partial \mathbf{U}} = \begin{bmatrix} \dfrac{\partial \mathbf{R}_0}{\partial \mathbf{U}_0} & \dfrac{\partial \mathbf{R}_0}{\partial \mathbf{U}_1} & \dfrac{\partial \mathbf{R}_0}{\partial \mathbf{U}_2} & \cdots & \dfrac{\partial \mathbf{R}_0}{\partial \mathbf{U}_{M-1}} \\[2mm] B\dfrac{\partial \mathbf{R}_0}{\partial \mathbf{U}_{M-1}}B^{-1} & B\dfrac{\partial \mathbf{R}_0}{\partial \mathbf{U}_0}B^{-1} & B\dfrac{\partial \mathbf{R}_0}{\partial \mathbf{U}_1}B^{-1} & \cdots & B\dfrac{\partial \mathbf{R}_0}{\partial \mathbf{U}_{M-2}}B^{-1} \\[2mm] \vdots & \vdots & \vdots & \cdots & \vdots \\[2mm] B^{M-1}\dfrac{\partial \mathbf{R}_0}{\partial \mathbf{U}_1}B^{-(M-1)} & \dfrac{\partial \mathbf{R}_0}{\partial \mathbf{U}_2}B^{-(M-1)} & \dfrac{\partial \mathbf{R}_0}{\partial \mathbf{U}_3}B^{-(M-1)} & \cdots & B^{M-1}\dfrac{\partial \mathbf{R}_0}{\partial \mathbf{U}_0}B^{-(M-1)} \end{bmatrix} \tag{7}$$

Next, the following change of variable is used:

$$\tilde{\mathbf{U}}_i = B^{-i}\mathbf{U}_i, \; \tilde{\mathbf{R}}_i = B^{-i}\mathbf{R}_i, \; i = 0, 1, 2, \ldots, M-1$$

9

The Jacobian then becomes

$$
\frac{\partial \mathbf{R}}{\partial \mathbf{U}} =
\begin{bmatrix}
\dfrac{\partial \tilde{\mathbf{R}}_0}{\partial \tilde{\mathbf{U}}_0} & \dfrac{\partial \tilde{\mathbf{R}}_0}{\partial \tilde{\mathbf{U}}_1} B^{-1} & \cdots & \dfrac{\partial \tilde{\mathbf{R}}_0}{\partial \tilde{\mathbf{U}}_{M-1}} B^{-(M-1)} \\[2ex]
B\dfrac{\partial \tilde{\mathbf{R}}_0}{\partial \tilde{\mathbf{U}}_{M-1}} & B\dfrac{\partial \tilde{\mathbf{R}}_0}{\partial \tilde{\mathbf{U}}_0} B^{-1} & \cdots & B\dfrac{\partial \tilde{\mathbf{R}}_0}{\partial \tilde{\mathbf{U}}_{M-2}} B^{-(M-1)} \\[2ex]
\vdots & \vdots & \cdots & \vdots \\[2ex]
B^{M-1}\dfrac{\partial \tilde{\mathbf{R}}_0}{\partial \tilde{\mathbf{U}}_1} & B^{M-1}\dfrac{\partial \tilde{\mathbf{R}}_0}{\partial \tilde{\mathbf{U}}_2} B^{-1} & \cdots & B^{M-1}\dfrac{\partial \tilde{\mathbf{R}}_0}{\partial \tilde{\mathbf{U}}_0} B^{-(M-1)}
\end{bmatrix}
\tag{8}
$$

$$
=
\underbrace{\begin{bmatrix}
I & 0 & \cdots & 0 \\
0 & B & \cdots & 0 \\
\vdots & \vdots & \cdots & \vdots \\
0 & 0 & \cdots & B^{M-1}
\end{bmatrix}}_{\mathcal{B}}
\underbrace{\begin{bmatrix}
\dfrac{\partial \tilde{\mathbf{R}}_0}{\partial \tilde{\mathbf{U}}_0} & \dfrac{\partial \tilde{\mathbf{R}}_0}{\partial \tilde{\mathbf{U}}_1} & \cdots & \dfrac{\partial \tilde{\mathbf{R}}_0}{\partial \tilde{\mathbf{U}}_{M-1}} \\[2ex]
\dfrac{\partial \tilde{\mathbf{R}}_0}{\partial \tilde{\mathbf{U}}_{M-1}} & \dfrac{\partial \tilde{\mathbf{R}}_0}{\partial \tilde{\mathbf{U}}_0} & \cdots & \dfrac{\partial \tilde{\mathbf{R}}_0}{\partial \tilde{\mathbf{U}}_{M-2}} \\[2ex]
\vdots & \vdots & \cdots & \vdots \\[2ex]
\dfrac{\partial \tilde{\mathbf{R}}_0}{\partial \tilde{\mathbf{U}}_1} & \dfrac{\partial \tilde{\mathbf{R}}_0}{\partial \tilde{\mathbf{U}}_2} & \cdots & \dfrac{\partial \tilde{\mathbf{R}}_0}{\partial \tilde{\mathbf{U}}_0}
\end{bmatrix}}_{\mathcal{A}}
\underbrace{\begin{bmatrix}
I & 0 & \cdots & 0 \\
0 & B^{-1} & \cdots & 0 \\
\vdots & \vdots & \cdots & \vdots \\
0 & 0 & \cdots & B^{-(M-1)}
\end{bmatrix}}_{\mathcal{B}^{-1}}
\tag{9}
$$

$$
= \mathcal{B}\mathcal{A}\mathcal{B}^{-1}
\tag{10}
$$

Therefore the Jacobian matrix is similar to a block-circulant matrix $\mathcal{A}$. As forementioned, matrix $\mathcal{A}$ has eigenvalues λ and eigenvectors $\mathbf{w}$. $\mathbf{w}$ is a compound vector formed by assemblying $\mathbf{v}$ with scalor factor ρ. The eigenvector of $\dfrac{\partial \mathbf{R}}{\partial \mathbf{U}}$ can be easily obtained by left multiplying the $\mathbf{w}$ with $\mathcal{B}$. Finally, the eigenvectors of the Jacobian matrix is

$$
\mathbf{w}_{m,n} = \left[\mathbf{v}_{m,n}, \rho_m B \mathbf{v}_{m,n}, \rho_m^2 B^2 \mathbf{v}_{m,n}, \ldots, \rho_m^{M-1} B^{M-1} \mathbf{v}_{m,n} \right]^T
$$

where $\mathbf{v}_{m,n}$ is the n-th eigenvector of

$$
\left(\frac{\partial \mathbf{R}_0}{\partial \mathbf{U}_0} + \rho \frac{\partial \mathbf{R}_0}{\partial \mathbf{U}_1} + \rho^2 \frac{\partial \mathbf{R}_0}{\partial \mathbf{U}_2} + \cdots + \rho^{M-1} \frac{\partial \mathbf{R}_0}{\partial \mathbf{U}_{M-1}} \right) \mathbf{v} = \lambda \mathbf{v}
$$

with $\rho = \rho_m$. It can be seen that for a given n, the M eigenvectors $\mathbf{w}_{0,n}, \mathbf{w}_{1,n}, \ldots, \mathbf{w}_{M-1,n}$ are modes with nodal diameters from 0 to $M - 1$, or $1 - M/2$ to $M/2$, provided that M is an even number.

D. Numerical implementation of eigenanalysis

In theory, performing the global linear stability analysis as described above is a standard procedure involving three steps: (i) find an equilirium point $\mathbf{u}_0$; (ii) linearize the nonlinear residual and form the Jacobian matrix A, and (iii) perform eigenanalysis and find Λ and V. Step (i) is simply running the steady state flow solver until a steady state solution is found. Step (ii) is a by-product of the nonlinear flow calculation using the NK method, i.e., store away the Jacobian matrix at the final Newton step. Step (iii) is a bit more involved for high dimensional problems.

10

For eigenmode computations, the implicitly restarted Arnoldi method proposed by Sorensen [8] and implemented in the ARPACK library [9], is used in combination with the NutsCFD solver. Shift-and-invert spectral transformation is applied to converge to wanted parts of the eigenspectrum, and critical is therefore the robust solution of many linear systems of equations. Key to efficiently solving the arising large sparse linear system of equations is the deflated Krylov subspace solver GCRO-DR [10]. Compared with the more commonly used GMRES solver [11], GCRO-DR is both more CPU time and memory efficient, especially as the system matrix condition worsens, as demonstrated in [12, 13].

IV. Results

A. Laminar flow around a two-dimensional circular cylinder

Eigenvalue analysis is performed for the canonical case of the laminar flow around a circular cylinder with the Reynolds number in the range between 40 and 100. The computational domain is a circular cylinder centered at the origin with a diameter of $D = 10^{-5}$ and the farfield is a circle with a diameter of $100D$. The left half of the outer circle is set to 'farfield' boundary condition with an incoming flow of Mach 0.2 in the x-direction, a static pressure of 101325 Pa and and a temperature of 288.15 K. The right half of the circle is set to 'pressure-outlet' boundary condition, with a constant pressure of 101325 Pa. The computational domain is meshed with quadrilateral elements, with a total of 29600 grid points. The density is 1.225 kg/m^3. The dynamic viscosity is varied in order to achieve a particular Reynolds number.

1. Steady state calculation

The steady state flow solution for $Re = 55$ is obtained by either using an implicit solution method in Fluent (version 19.2) or by resorting to the Newton-Krylov algorithm in NutsCFD, despite the fact that the flow is physically unsteady under this condition. The Mach number contour of the NutsCFD calculation is shown in Fig. **??**.

To compare the Fluent and NutsCFD results quantitatively, the x-velocity behind the cylinder and the pressure coefficient along the cylinder surface are presented in Fig. 3 and very good agreement can be found.

2. Unsteady calculation

Experimental results show that the laminar flow around the cylinder becomes unsteady for Re above a critical value (around 47)[14]. To study this phenomenon, unsteady flows for $Re = 55$ and $Re = 40$ are performed using NutsCFD. First, for both conditions, a steady state flow solution is obtained by converging the residual to machine error. Then, unsteady simulation is run with the steady state as the initial condition for $Re = 55$. A BDF2 second-order implicit dual-time-stepping method is used with the physical time step set to $10^{-8} sec$, that is, $0.01ms$, and the inner loop is solved with a maximum of 3 Newton iterations. From Fig. 4, it can be seen that after around $100ms$, the lift coefficient starts to grow and eventually reaches a saturated limit cycle at around $130ms$. On the contrary, running unsteady simulation
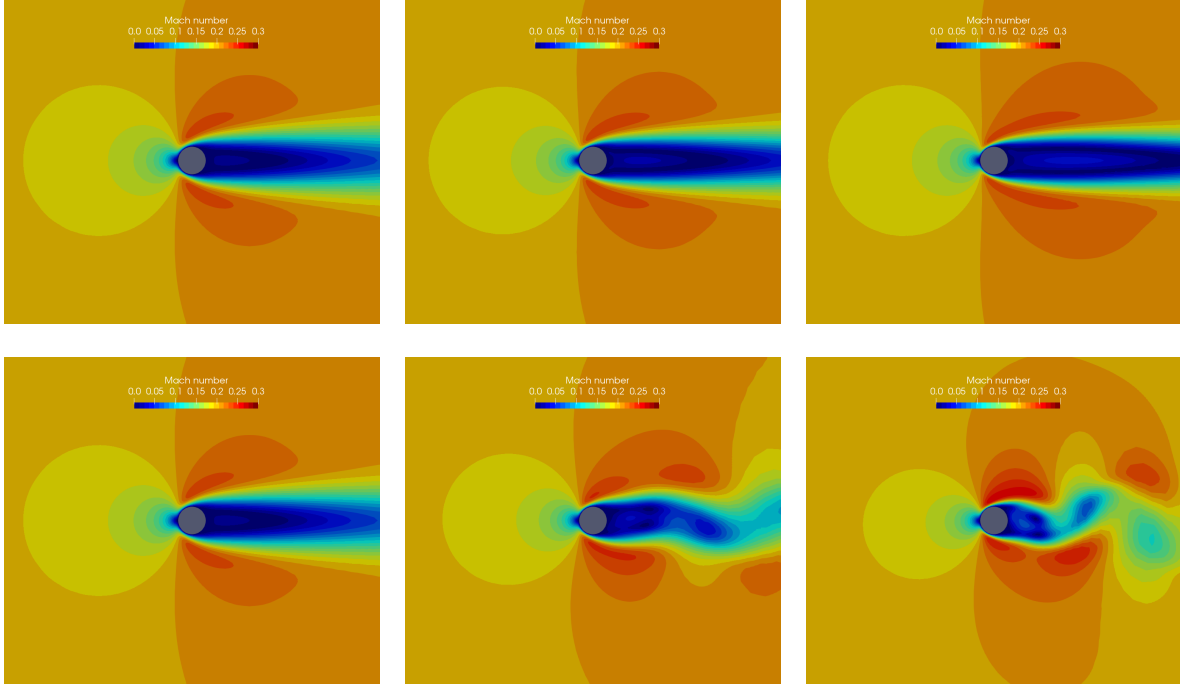
11

Fig. 3   From left to right: Re=40, 60, 100. Upper: steady state solution; lower: unsteady solution snapshot.

with a fully converged steady state for $Re = 40$ does not lead to unsteadiness. To probe the flow at $Re = 40$ further, a disturbance is introduced into the flow from the farfield by setting the incoming flow direction to vertical for one time step and switching it back to the x-direction, and then continue the unsteady run. The lift coefficient shows a transient growth but eventually slowly delays to zero. The two sets of lift coefficient signals for $Re = 40$ and $Re = 55$ are plotted in Fig. 4 in both linear and logrithm scales. The logrithmic plot on the right clearly shows an exponential growth/decay for $Re = 55$ and $Re = 40$, respectively.
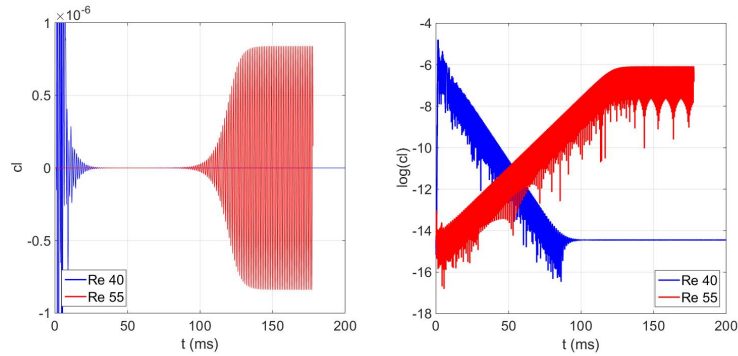
Fig. 4   Lift coeffient histogram for $Re = 55$ and $Re = 40$.

3. Eigenanalysis

Eigenanalysis is performed for the steady state solution calculated using NutsCFD. After converging the steady state solver to machine error ($tol = 10^{-14}$), the exact Jacobian matrix based on the 2nd-order spatial accuracy is calculated and output to file. ARPACK is used to computed a subset of the eigenvalues, with the aim of finding the least stable mode. To minimize the computational effort, 10 eigenvalues/vectors are computed for matrices with different shifts of 0, i, $2i$, $3i$, $4i$, $5i$. All the eigenvalues, 60 in total and with some duplicated, are plotted in Fig. 5. It can be seen that there is one eigenvalue that is on the right side of the imaginary axis, indicating there is one unstable mode. In the meantime, from the time-domain simulation, one can extract from the lift-coefficient signal that the flow is exponentially growing with a growth rate of 0.123 and oscillating with a circular frequency of 4.94 rad/s. This value is plotted along with the spectrum and it can be seen that it overlaps with the unstable eigenvalue from the eigenanalysis.
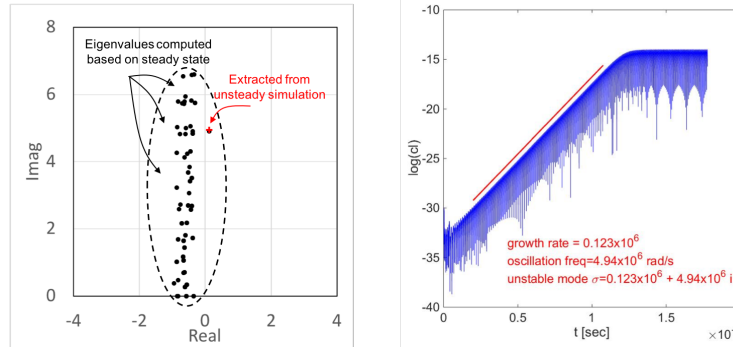

Fig. 5   Eigenspectrum from the steady state eigenvalue analysis compared with the linearly destabiling unsteady simulation for $Re = 55$**.**

The eigenanalysis not only generates the eigenvalues but also the eigenvectors associated with each eigenvalue. For the unstable mode, the real part of the density, x/y momentum and energy component of the unstable eigenvector is shown in Fig.6. Although not further explored here, these eigenvectors will be useful for constructing reduced-order-models, which can be used for rapid parametric study or fast time-domain responce.
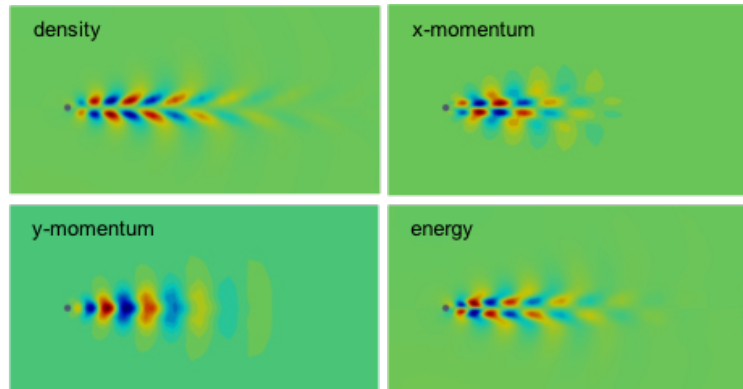

Fig. 6   Real part of the density, x/y momentum, energy components of the unstable eigenmode for $Re = 55$**.**
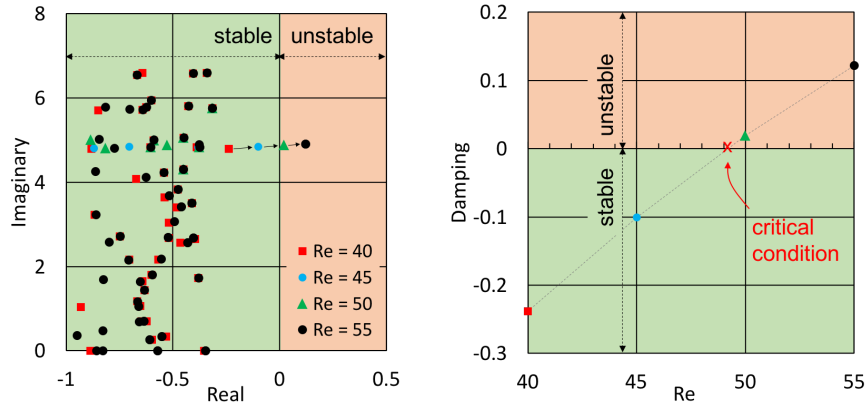
13

4. Bifurcation tracking

Fig. 7   The spectra for $Re = 40, 45, 50$ **and** 55 **(left) and the damping v.s. the Reynolds number (right).**

The same procedure for computing the eigenvalues for $Re = 55$ is applied to flows at $Re = 40$, 45, and 50 to obtain their respective spectra, which is shown in Fig. 7. It can be seen that as the bifurcation parameter Re is increased from 40 to 55, one eigenmode becomes linear unstable. The real part of this eigenvalue is plotted against Re on the right in Fig. 7. It across the imaginary axis at approximately $Re = 49$, consistent with the experimental value of $Re_{crit} = 47$. Note that shown in the figure is only the upper half of the spectrum and the complex conjugate of the destabilizing eigenvalue is thus not visualized. This is a classic Hopf bifurcation as the conjugate complex eigenpair destabilizes simultaneously. However, it should be noted that although linear stability analysis can predict the exact bifurcation, frequency predicted based on the unstable eigenvalue beyond that critical bifurcation parameter, Re_{crit}, should be used with care as it is different from the vortex shedding frequency except very close to onset, for the laminar flow around a long cylinder [15]. The implication on general cases is yet to be explored in future work.

B. Singlerow annular cascade (quasi-3D analysis)

NutsCFD is used to analyze the performance of the first stage rotor (NASA Rotor 67) of a two stage transonic fan designed and tested at the NASA Glenn center [16]. Its design pressure ratio is 1.63, at a mass flow rate of 33.25 kg/sec. The NASA Rotor 67 has 22 blades with tip radii of 25.7 cm and 24.25 cm at the leading and trailing edge, respectively, and a constant tip clearance of 1.0 mm. The hub to tip radius ratio is 0.375 at the leading edge (TC = 0.6% span) and 0.478 at the trailing edge (TC = 0.75% span). The design rotational speed is 16,043 RPM, and the tip leading edge speed is 429 m/s with a tip relative Mach number of 1.38.

As a first step, the analysis is performed on the surface of revolution taken at approximately 50% of the blade height. The three-dimensional mesh has one cell in the radial direction and the subsequent analysis is thus a quasi-3D one.

14

1. Steady state calculation

Steady state analysis is first performed for an annular compressor cascade. The pressure ratio and efficiency against the mass flow normalized by the choked mass flow, produced by incrementally raising the back pressure, are shown in Fig. **??**. The fully-converged steady state flow solution scorresponding to the lowest and highest back pressures are shown in Fig. 9.
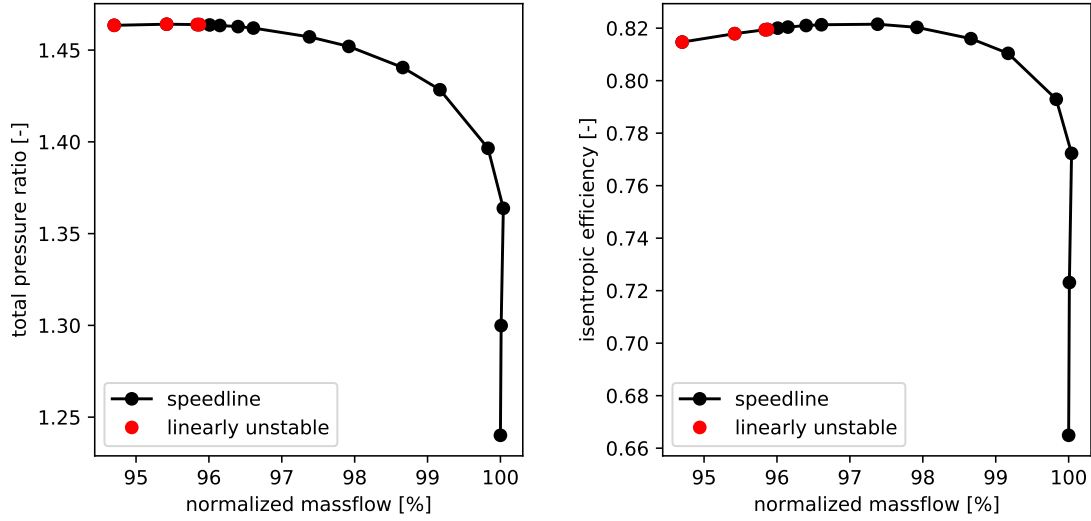

Fig. 8

2. Eigenanalysis

Eigenvalue analysis is performed for all the steady state solutions along the speedline. Since only the 'relevant' eigenvalues are desired (relevant here means eigenvalues that are likely to across the imaginary axis, corresponding to the onset of Hopf-bifurcation), the knowledge that the rotating stall cells usually move along the circumferential direction with a speed that is on the same order of the rotating rotation speed, each element of the Jacobian matrix is therefore divided by a factor of $1/(2\pi \times 16043/60) \approx 1/1680$ (assuming the rotational speed of 16,043 RPM), so that the frequency information represented by the imaginery part of the eigenvalues found is in terms of engine order (EO).

For each condition in Fig. 9, the relevant eigenvalues are computed by applying shifts of $\sigma = 0 + 0.5j, 0 + 1j, 0 + 1.5j$ and $0 + 2j$ to the Jacobian matrices and finding the 10 most interior eigenvalues of the shifted matrices.

3. Interpretation of the eigenanalysis results

Shown in Fig. 10 is a subset of the eigenvalues that are near the imaginary axis, which presumally are most likely to be unstable. ARPACK is used with various imaginery shifts to compute interior eigenvalues. The ones that are suspicious of crossing the imaginery axis are shown. A zoomed view of the eigenvalues reveals that there are a total of
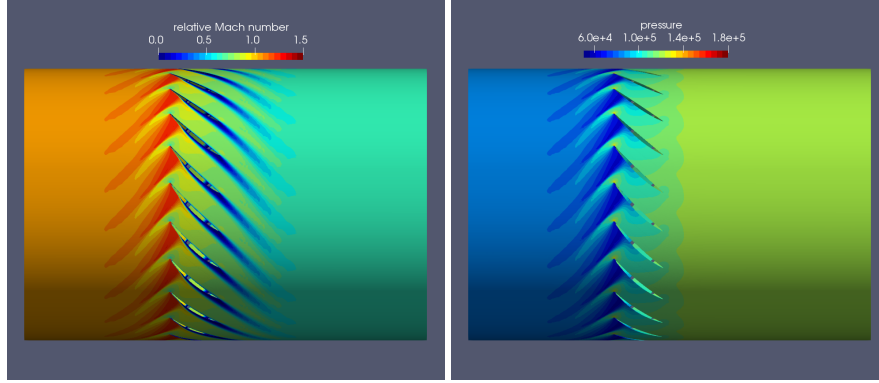
15

choked condition
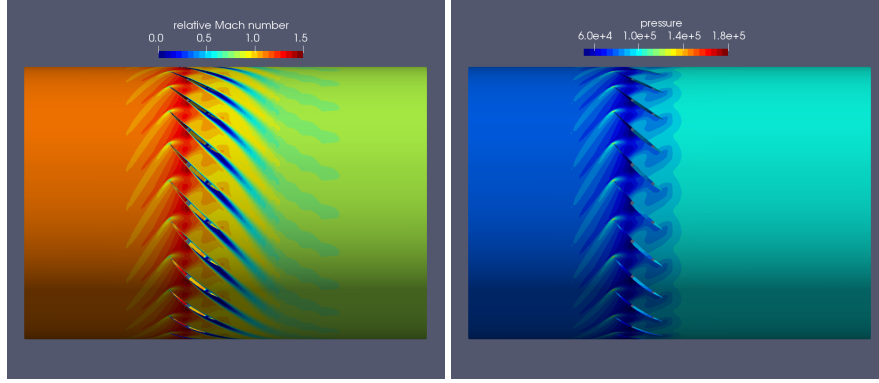
near stall condition

Fig. 9   Pressure (left) and SA variable (right) contours for whole-annulus calculations.

five that have positive real parts, i.e., unstable. A single-mode instability is not found for the case most likely because the flow condition chosen is one that is deep into the linearly unstable region and a bifurcation point should be searched for at a higher flow-rate condition. Nevertheless, in the work, we restrict outselves to the analysis of this single condition and a thorough exploration of the whole picture will be conducted in our future work.

The unstable eigenvector with the smallest imaginary part (lowest point among the five unstable eigenvalues) is visualized in Fig. 12 with both the real and imaginary parts. The circumferential shock oscillation can be seen. To analyze the spatial modes, data along the intersecting curve is taken (marked at the red line in Fig. 12). This is done for each of the 11 modes (marked with red cross in Fig. 10). It is clear from the spatial Fouriour analysis that each eigenvector corresponds to a rotating pattern with a different nodal diameter, which increases from 1 to 11 monotonically from the lowest to the highest eigenvalues.

A more involved data processing reveals that the perturbation pattern, for every eigenvector, is a travelling wave that rotates in the opposite direction of the motion of the rotor (in the relative frame), and with a speed a fraction of the shaft rotating speed. This relative rotating speed can be calculated using the imaginary of the eigenvalue and the nodal
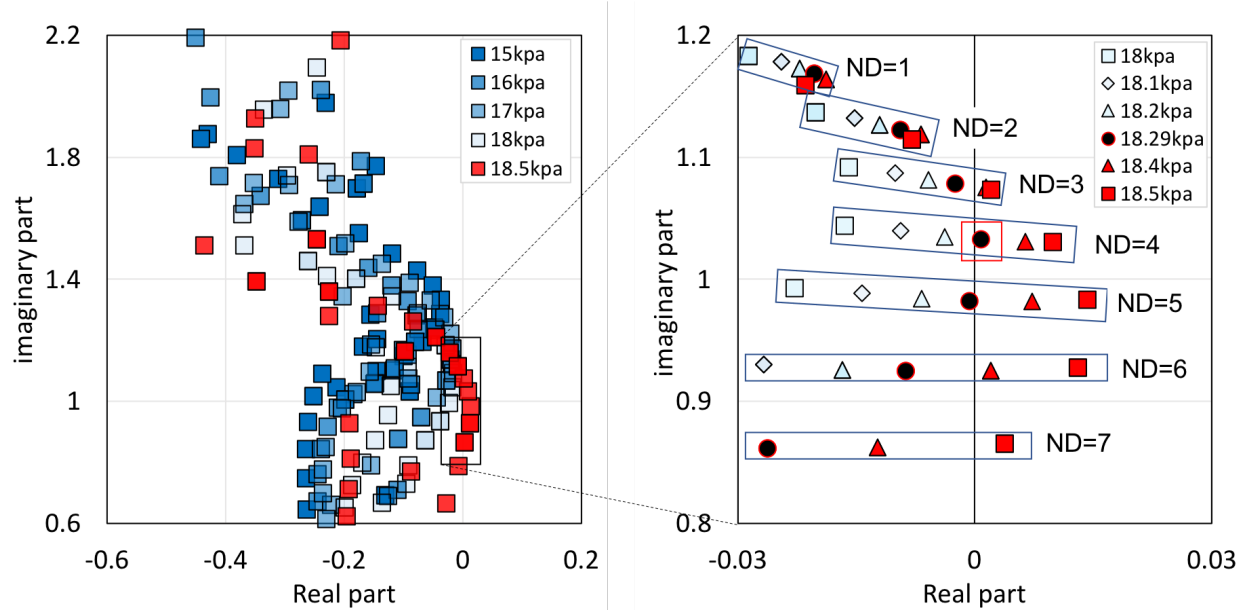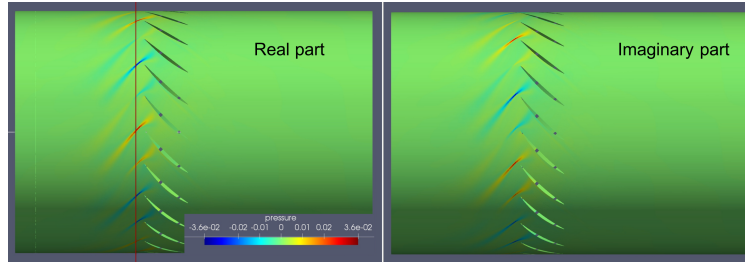
Fig. 10   Spectrum for stall condition.

Fig. 11   Eigenvector 5 visualized using the real and imaginary parts of energy component

diameter of the perturbation pattern as

$$\Omega^{rel}_{cellRotation} = \frac{\mathrm{Imag}(\lambda)}{ND}\Omega_{shaft} \tag{11}$$

In the absolute reference frame, the cell rotating speed (normalized with shaft angular frequency) is calculated as

$$\Omega^{abs}_{cellRotation} = \left(1 - \frac{\mathrm{Imag}(\lambda)}{ND}\right)\Omega_{shaft} \tag{12}$$

Applying this formula to each of the 11 eigenmodes leads to the correlation between the nodal diameter and the perturbation rotating speed, as shown in Fig. 12. Note that we use the terminology 'cell rotating speed' to be consistent with the language used by experimentalists when they describe the rotating cells. In fact, what is meant in the current context is actually 'rotating speed of the perturbation pattern'. Although it is well-known that the conclusions drawn from a global linear stability analysis can not represent the behavior of a saturated limit cycle which is highly

17

nonlinear, it seems that the characteristics of the rotating perturbation, in terms of nodal diameter and rotating speed, is qualitatively representative of rotating cells observed experimentally. However, questions such as which eigenmode should destabilizes first, and how does the inlet distortion and blade-row interaction in multirow configuration affect the conclusion, remain to be answered.
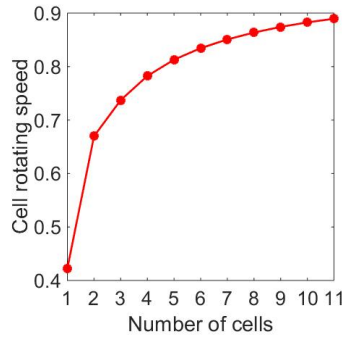

Fig. 12   The cell rotating speed in the absolute frame of reference v.s. the number of cells (nodal diameter of the perturbation pattern).

4. Unsteady analysis

C. Rotor 67

Update performance curve with data at the correct survey station location.

1. Case overview

The final case is the NASA Rotor 67 transonic fan, which is the first-stage rotor of a two-stage transonic fan. It has 22 low aspect-ratio blades and was designed for a rotational speed of 16,043 rpm, with a total pressure ratio of 1.63 and a mass flow of 33.25 kg/s [**?**]. The flow calculations for this case are performed using 72 processors.

2. Accuracy validation

The computational domain with a single blade passage is meshed with 973,065 grid points and 934,400 hexahedral elements. The height of the first layer cell off the viscous wall is 10^{-6} m, satisfying $y^+ \approx 1$. The geometry of the rotor blade as well as detailed views of the mesh are shown in Fig. 13.

At the inlet boundary, a total pressure of 101325 Pa and a total temperature of 288.15 K are imposed. The incoming flow is in the axial direction. Since the outlet boundary is relatively far from the rotor, i.e., the distance from the rotor trailing edge to the outlet boundary is over twice the chord length, a constant back pressure is imposed at the outlet as the boundary condition. Our numerical experiment shows that using a radial equilibrium boundary condition only changes the resulting speedline negligibly. Therefore, the constant back pressure boundary condition is used for simplicity. The back pressure is set to 0 kPa initially and then gradually raised to produce the speedline. The procedure illustrated in
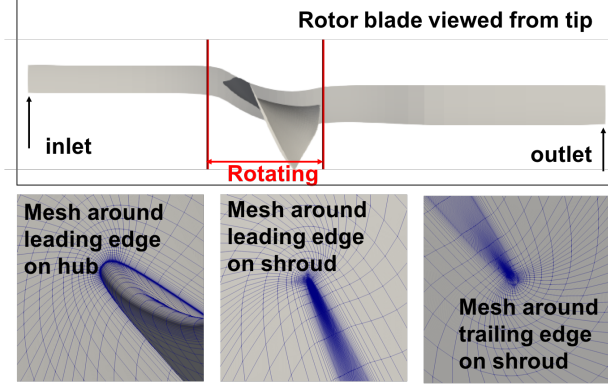
Fig. 13 **NASA rotor 67 blade viewed from the tip (top) and detailed views of the computational mesh (bottom). The rotating part of the hub surface, from $x = -1.374$ cm to $x = 9.365$ cm, is marked with the two vertical lines.**

Fig. **??**, is used to generate the speedline, except that for this case, pressure increments of 5 kPa, 1 kPa and 0.1 kPa are used.

The experimental and numerical speedlines are shown in Fig. 14 for comparison. The relative error for the choked flow rate is 1.0%, which is similar to reported values of other numerical investigations [**?**]. The under-prediction of the pressure ratio and the efficiency is suspected to be caused by the fact that the implementation of the S-A turbulence model used here is not fully appropriate for this case. However, as this work focuses on the solver convergence and robustness, this is not further investigated here.
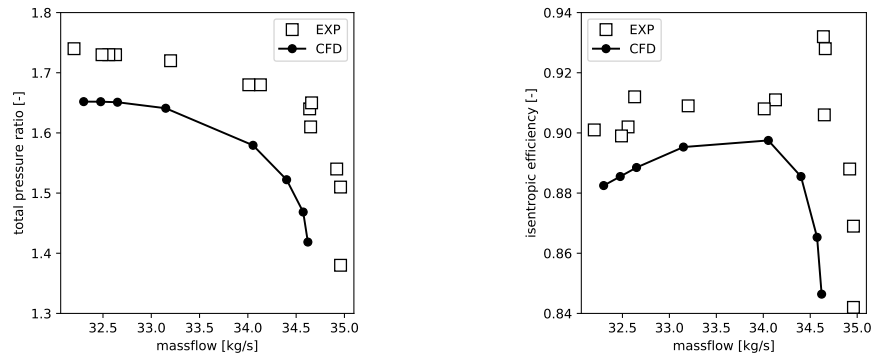

Fig. 14 **CFD calculations compared with measurements [?] for NASA Rotor 67.**

V. Conclusion

Rotating flow instability at near stall condition for an annular compressor cascade is studied using the eigenanalysis approach and the destabilizing eigenmodes are computed and analyzed to shed insight on the rotating stall phenomenon. This is the first time a full-order gloabl linear stability analysis based on the three dimensional RANS equations is performed to study the destabilising mechanism of such turbomachinery flow phenomenon.

19

Specifically, a stable nonlinear flow solver based on the matrix-forming Newton–Krylov approach is used to compute the steady state flow solution at near stall (possibly post-stall) condition and the readily available exact Jacobian matrix is then used for eigenvalue anlaysis. The eigenanalysis is performed to compute a subset of the eigenvalues that are near the imaginary axis, with the implicit-restarted Arnoldi method implemented in the ARPACK library. The shift-and-invert approach is used to obtain the least unstable eigenvalues.

The methodology is first applied to the classic case of a laminar flow around a 2D circular cylidner. By perturbing the system parameter *Re*, Hopf bifurcation is identified which is responsible for the inception of the laminar vortex shedding. The frequency and linear growth ratio from the eigenanalysis agree well with time-dependent simulation during the linear growth regime.

The same procedure is then applied to the a quasi-3d compressor rotor. Analysis shows the existance of a complete set of spatial modes that have different nodal diameters and rotating speeds. These analysis results provide a solid foundation for the explanation of various observations in experiments regarding rotating flow instabilities. It is revealed that the multiple modes with different nodal diameters coexist, as the inherent property of the physical system, and it can be hypothesized that the reason for different observed stall cell patterns is due to one particular mode being excited to finite amplitute first by external disturbance. Further more, by processing the spatial modes and the imaginary part of the eigenvalues, rotating speeds of the perturbation patterns can be calculated and are found to qualitatively agree with the various experimentally observed values for rotating stall cells.

The preliminary results presented in this paper represent our first attempt to use eigenanalysis based on RANS equations to study the rotating flow instability phenomenon in turbomachinary flows. The results are promising in that it shows the eigenanalysis method is feasible for practical cases and the eigenvectors do capture some of the key featuers of the flow instability investigated. However, more in-depth study is needed to investigate the bifurcation process for the quasi-3D case, and further investigation into three-dimensional cases will be carried out in our future work.

Acknowledgements

References

[1] Xu, S., Mohanamuraly, P., Wang, D., and Müller, J.-D., "Newton–Krylov Solver for Robust Turbomachinery Aerodynamic Analysis," *AIAA Journal*, 2019, pp. 1–17.

[2] Xu, S., Mohanamuraly, P., Wang, D., and Müller, J.-D., "A parallel Newton–Krylov RANS solver for turbomachinery aerodynamic analysis at off-design conditions," *submitted*, 2019.

[3] Allmaras, S. R., and Johnson, F. T., "Modifications and clarifications for the implementation of the Spalart–Allmaras turbulence model," *Seventh international conference on computational fluid dynamics (ICCFD7)*, 2012, pp. 1–11.

[4] Spalart, P. R., and Allmaras, S. R., "A one equation turbulence model for aerodinamic flows," AIAA-CP 92-439, 1992.

[5] Langer, S., "Agglomeration multigrid methods with implicit Runge–Kutta smoothers applied to aerodynamic simulations on unstructured grids," *Journal of Computational Physics*, Vol. 277, 2014, pp. 72–100.

[6] Hascoët, L., and Pascual, V., "The Tapenade Automatic Differentiation tool: Principles, Model, and Specification," *ACM Transactions On Mathematical Software*, Vol. 39, No. 3, 2013.

[7] Gebremedhin, A. H., Nguyen, D., Patwary, M. M. A., and Pothen, A., "ColPack: Software for graph coloring and related problems in scientific computing," *ACM Transactions on Mathematical Software (TOMS)*, Vol. 40, No. 1, 2013, p. 1.

[8] Sorensen, D. C., "Implicit application of polynomial filters in a k-step Arnoldi method," *SIAM journal on matrix analysis and applications*, Vol. 13, No. 1, 1992, pp. 357–385.

[9] Lehoucq, R. B., Sorensen, D. C., and Yang, C., *ARPACK users' guide: solution of large-scale eigenvalue problems with implicitly restarted Arnoldi methods*, Vol. 6, SIAM, 1998.

[10] Parks, M., de Sturler, E., Mackey, G., Johnson, D., and Maiti, S., "Recycling Krylov subspaces for sequences of linear systems," *SIAM Journal on Scientific Computing*, Vol. 28, No. 5, 2006, pp. 1651–1674.

[11] Saad, Y., and Schultz, M., "GMRES: A generalized minimal residual algorithm for solving nonsymmetric linear systems," *SIAM Journal on scientific and statistical computing*, Vol. 7, No. 3, 1986, pp. 856–869.

[12] Xu, S., Timme, S., and Badcock, K., "Enabling off-design linearised aerodynamics analysis using Krylov subspace recycling technique," *Computers & Fluids*, Vol. 140, 2016, pp. 385–396.

[13] Xu, S., and Timme, S., "Robust and efficient adjoint solver for complex flow conditions," *Computers & Fluids*, Vol. 148, 2017, pp. 26–38.

[14] Williamson, C. H. K., "Vortex Dynamics in the Cylinder Wake," *Annual Review of Fluid Mechanics*, Vol. 28, No. 1, 2003, pp. 477–539.

[15] Barkley, D., "Linear analysis of the cylinder wake mean flow," *Europhysics Letters*, Vol. 75, No. 5, 2006, p. 750.

[16] Strazisar, A. J., Wood, J. R., Hathaway, M. D., and Suder, K. L., "Laser anemometer measurements in a transonic axial-flow fan rotor," 1989.